

# Electrically controlling and optically observing the membrane potential of supported lipid bilayers

Shimon Yudovich,<sup>1,2,\*</sup> Adan Marzouq,<sup>2,3</sup> Joseph Kantorovitch,<sup>2</sup> Eti Teblum,<sup>2</sup> Tao Chen,<sup>4</sup> Jörg Enderlein,<sup>4,5</sup> Evan W. Miller,<sup>6</sup> and Shimon Weiss<sup>1,2,7,\*</sup>

<sup>1</sup>Department of Physics, Bar-Ilan University, Ramat-Gan, Israel; <sup>2</sup>Institute for Nanotechnology and Advanced Materials, Bar-Ilan University, Ramat-Gan, Israel; <sup>3</sup>Department of Chemistry, Bar-Ilan University, Ramat-Gan, Israel; <sup>4</sup>Third Institute of Physics–Biophysics, Georg August University, Göttingen, Germany; <sup>5</sup>Cluster of Excellence “Multiscale Bioimaging: from Molecular Machines to Networks of Excitable Cells” (MBExC), Georg August University, Göttingen, Germany; <sup>6</sup>Departments of Chemistry, Molecular & Cell Biology, and Helen Wills Neuroscience Institute, University of California, Berkeley, California; and <sup>7</sup>Departments of Chemistry and Biochemistry, Physiology, and California NanoSystems Institute, University of California Los Angeles, Los Angeles, California

**ABSTRACT** Supported lipid bilayers are a well-developed model system for the study of membranes and their associated proteins, such as membrane channels, enzymes, and receptors. These versatile model membranes can be made from various components, ranging from simple synthetic phospholipids to complex mixtures of constituents, mimicking the cell membrane with its relevant physiochemical and molecular phenomena. In addition, the high stability of supported lipid bilayers allows for their study via a wide array of experimental probes. In this work, we describe a platform for supported lipid bilayers that is accessible both electrically and optically, and demonstrate direct optical observation of the transmembrane potential of supported lipid bilayers. We show that the polarization of the supported membrane can be electrically controlled and optically probed using voltage-sensitive dyes. Membrane polarization dynamics is understood through electrochemical impedance spectroscopy and the analysis of an equivalent electrical circuit model. In addition, we describe the effect of the conducting electrode layer on the fluorescence of the optical probe through metal-induced energy transfer, and show that while this energy transfer has an adverse effect on the voltage sensitivity of the fluorescent probe, its strong distance dependency allows for axial localization of fluorescent emitters with ultrahigh accuracy. We conclude with a discussion on possible applications of this platform for the study of voltage-dependent membrane proteins and other processes in membrane biology and surface science.

**SIGNIFICANCE** We introduce a novel platform as a testbed for the development of optical membrane potential sensors for electrophysiology and bioelectricity applications. The platform is based on supported lipid bilayers (SLBs) that are accessible both electrically and optically. The equivalent electrical circuit of the system is characterized by electrochemical impedance spectroscopy, which allows us to fully and precisely describe the dynamics of the electrical system. Voltage-sensitive dyes are used to optically monitor the membrane potential, showing good agreement between the two orthogonal approaches. In addition, we describe the effect of the electrode on the emission of the fluorescent probe through metal-induced energy transfer. The platform can allow for novel voltage-dependent experiments for the study of membrane and membrane protein biophysics.

## INTRODUCTION

Biological membranes are a main component of life, providing cells and membrane-enclosed organelles compartmentalization, together with functional, communicational, and computational capabilities. By utilizing

various phospholipids, glycolipids, cholesterol, and proteins, complex lipid bilayers acquire different physiochemical and molecular properties that allow for intricate functions, such as chemical and electrical gating, signal transduction, and catalysis. Among several model lipid bilayer systems, supported lipid bilayers (SLBs) (1,2) offer an extremely versatile and robust platform for the study and application of membranes and associated lipids and proteins (3–5).

At their simplest form, SLB systems are composed of phospholipids deposited on top of a solid support to make

Submitted December 12, 2021, and accepted for publication May 23, 2022.

\*Correspondence: [shimon.yudovich@gmail.com](mailto:shimon.yudovich@gmail.com) or [sweiss@chem.ucla.edu](mailto:sweiss@chem.ucla.edu)

Editor: Tommy Nylander.

<https://doi.org/10.1016/j.bpj.2022.05.037>

© 2022 Biophysical Society.

This is an open access article under the CC BY-NC-ND license (<http://creativecommons.org/licenses/by-nc-nd/4.0/>).



a continuous planar bilayer. Planar bilayer formation can be achieved by, for example, the Langmuir-Blodgett technique (6,7), the adsorption and fusion of vesicles (8) or bicelles (9), or by gradual organic to water solvent exchange (10). The physiochemical properties of the supported bilayer, such as its phase and fluidity, will be determined by the composition of the bilayer (11) and the properties of the underlying substrate (12). These properties, in turn, can influence the structure and functionality of embedded proteins. In addition, nuclear magnetic resonance (13), neutron (14), and x-ray reflectometry (15) showed that a hydration layer of 5–30 Å in thickness is present between the substrate and bilayer, influencing the fluidity of the lower leaflet. The artificial interface occurring at the leaflet closer to the support can prevent membrane proteins with extracellular domains to be fully functional, as they can become immobilized and denatured due to the interaction between the protruding hydrophilic domain and the nonphysiological underlying environment (3). To lessen the adverse effects of the artificial solid support, hydrated polymer films can be deposited on the support before bilayer formation (16,17). In addition to cushioning polymer films, many approaches for tethering lipid bilayers to the solid support have been developed (18). For example, DNA-lipid conjugates can be used to distance the bilayer from the solid support in a controllable manner (19). Due to the high stability of SLBs, many experimental techniques can be applied to study the membrane and its associated biomolecules. In particular, the electrochemical properties of SLBs were thoroughly studied using different supporting substrates, such as doped silicon (20,21), silicon-silicon dioxide (22), indium tin oxide (ITO) (21,23–25), titanium-titanium dioxide (26), gold (21), gold-silicon dioxide (27,28), and semi-conducting polymers (29). By incorporating ion channels in electrically accessible SLBs, one can record ionic currents flowing through these channels and characterize the dependence of their conductance on various parameters, such as the applied voltage and surrounding ligands. By converting molecular recognition events to measurable electrical signals, such systems can be utilized as a versatile platform for highly sensitive biosensors (30–34).

The electrical potential across a lipid bilayer dictates many of its functional properties and is commonly defined over three main regions (35–37): 1) The potential arising from the charged headgroups and adsorbed ions at the membrane-liquid interface (surface potential). 2) The potential produced by the aligned molecular dipoles of both lipids and water at the interface (dipole potential). 3) The overall potential difference due to the different ion concentrations on both sides of the membrane (transmembrane potential). Transmembrane potential plays a main role in the communicational and computational capabilities of cells through its effect on membrane proteins. An important and highly studied class of membrane proteins is voltage-gated ion channels. These transmembrane proteins contain voltage-sensing gate

domains that translocate due to applied electric fields, thus regulating ion conductance (38,39). Beyond voltage-gated ion channels, numerous transporters (40) and enzymes (41,42) are directly affected by the transmembrane potential. In addition, it is very likely that many proteins and processes in the membrane are affected or induced by the electrical potential across the membrane (43,44). In particular, microscopic electrostatics can direct the conformation and function of membrane proteins through their charged domains (45,46).

In this work, we describe a platform for SLBs that is addressable both electrically and optically. We characterize the electrical response of the bilayer with electrochemical impedance spectroscopy (EIS) (47) and demonstrate the ability to electrically polarize SLBs while optically monitoring their membrane potential using voltage-sensitive membrane dyes. We show that the optically measured changes in membrane potential can be understood through the dynamical properties of an equivalent electrical circuit model. This work shows for the first time, to our knowledge, the correspondence between two orthogonal experimental techniques (EIS and fluorescence spectroscopy) for the study of SLB electrostatics. In addition, we describe the effect of the conducting electrode layer on the radiative transition of the demonstrated membrane dye through metal-induced energy transfer (MIET) (48,49), and discuss its implications on fluorescence-based measurements performed on electrode-supported SLBs. Finally, we present possible future applications for this platform, emphasizing the complementarity between optical and electrochemical techniques and their relevance in the study of voltage-dependent membrane proteins and other voltage-dependent processes and phenomena in molecular biology and surface science.

## MATERIALS AND METHODS

### Metal-oxide substrate

Glass coverslips (Marienfeld Superior, Lauda-Königshofen, Germany) coated with a layer of ~8 nm Ti and ~20 nm Ta<sub>2</sub>O<sub>5</sub> served as an optically transmissive metal-oxide substrate for the lipid bilayer for all the experiments described in this work, apart from Figs. 5 and S4, where varying thicknesses of Ta<sub>2</sub>O<sub>5</sub> were used. Deposition of both Ti and Ta<sub>2</sub>O<sub>5</sub> layers was performed using an ion beam sputtering technique (Nanoquest I; Intlvac, Ontario, Canada). For the Ti layer, a stainless steel mask (3 mm in diameter) was used to define the surface area of the electrode. Ti was sputtered from a Ti target at an average sputtering rate of ~1 Å/s, using a sputtering ion beam voltage of 1200 V and beam current of 120 mA, with Ar (10 sccm) as the working gas. Ta<sub>2</sub>O<sub>5</sub> was sputtered from a Ta target at an average sputtering rate of ~0.9 Å/s, using a sputtering ion beam voltage of 1200 V and beam current of 110 mA, with Ar (10 sccm) as the working gas, and an assisting ion source composed of Ar (10 sccm) and O<sub>2</sub> (18 sccm) at an ion beam voltage of 120 V and beam current of 95 mA. Substrate roughness characterization was performed in air with atomic force microscopy (AFM). AFM measurements were carried out using a scanning probe microscope (Bio FastScan; Bruker, Karlsruhe, Germany). All images were obtained using soft tapping mode with a silicon probe (Fast Scan B; Bruker) with a spring constant of 1.8 N/m. The resonance

frequency of the cantilever was approximately 450 kHz (in air). The images were captured in the retrace direction with a scan rate of 1.6 Hz, with a resolution of 512 samples per line. Image processing and roughness analysis were performed using a dedicated open-source software (Gwyddion) (50).

## Lipid vesicle preparation

Homogenous lipid vesicles were prepared by hydration of a dry lipid mixture, followed by sonication and extrusion. In short, 530 nmol of 1-palmitoyl-2-oleoyl-glycero-3-phosphocholine (POPC) (Avanti Polar Lipids, Alabaster, AL) and 150 nmol of 1-palmitoyl-2-oleoyl-sn-glycero-3-phospho-L-serine (POPS) (Avanti Polar Lipids) were dissolved in chloroform and mixed in a molar proportion of approximately 80 and 20%, respectively, evaporated for 1 h at 40°C using a centrifugal vacuum concentrator (CentriVap Concentrator; Labconco, Kansas City, MO), and dried under vacuum overnight. The lipid film was dispersed in 1 mL of Tris-NaCl buffer (10 mM Tris, 100 mM NaCl [pH 8]), giving a final lipid concentration of ~0.6 mM. The solutions were sonicated using a probe sonicator for 30 s at 26 Watt, 20 kHz (VCX 130; Sonics, Newtown, CT). Afterward, the lipid solutions were centrifuged for 20 min at  $16,000 \times g$  and 4°C. The suspensions were then extruded (Mini-Extruder; Avanti Polar Lipids) 11 times through 100 nm polycarbonate membranes (Nuclepore Hydrophilic Membrane; Whatman, Clifton, NJ). The hydrodynamic size distribution of the vesicles at each step was measured using dynamic light scattering (Zetasizer Nano ZS; Malvern Instruments, Westborough, MA) using a 633 nm laser and a scattering angle of 173°, operating at 25°C (Fig. S1). To ensure repeatability between preparations, the total scattered intensity was used as an indicator for the vesicle concentration.

## Supported lipid bilayer formation

A POPC:POPS lipid bilayer with an overall negative surface charge was prepared by the rupturing and fusing of lipid vesicles on the hydrophilic metal-oxide substrate. We found that, using the following SLB formation procedure, a POPC:POPS lipid mixture forms more fluid SLBs compared with SLBs from POPC alone. In addition, the use of such constituting lipids better mimics the overall negative surface charge of biological membranes in physiological conditions (51). Substrates were first cleaned by 5 min sonication in detergent solution (2% Hellmanex III; Hellma, Müllheim, Germany), double-distilled water (DDW), and acetone. Next, the substrates were rinsed with DDW and dried under a stream of N<sub>2</sub>. To ensure a high

degree of hydrophilicity, substrates were further treated under a glow discharge system (Emtech K100×; Quorum Technologies, Sussex, UK) for a total of 5 min. Next, a disposable polylactic acid chamber (shown in Fig. 1 A) was attached on top of the treated substrate using a silicone sealant glue. The experimental chamber was immediately transferred to a vacuum desiccator for 20 min, allowing the sealing agent to dry while keeping the treated electrode surface unaffected by humidity. Next, 50 μL of the vesicle solution was added to the chamber, together with Tris-NaCl buffer containing CaCl<sub>2</sub> for a final concentration of 2 mM CaCl<sub>2</sub>. The vesicles were allowed to incubate for 20 min, followed by multiple buffer exchanges for the removal of unbound vesicles. While membrane resistance  $R_m$  was found to be variable between preparations, the likelihood of achieving high  $R_m$  considerably increased for membranes that were allowed to stabilize at room temperature for 16–24 h after the removal of unbound vesicles. SLBs were stained with VF2.0.Cl or VF2.1.Cl shortly before experiments by incubating the SLB for 5 min in a buffer solution containing the membrane dye at a final concentration of 100 nM. Following incubation with the membrane dye, multiple buffer exchanges were performed to remove free dye from the buffer solution.

## EIS

Electrochemical characterization and control were performed in a three-electrode cell configuration using a commercial potentiostat (Autolab PGSTAT302N; Metrohm, Utrecht, the Netherlands), with the conductive Ti substrate connected as the working electrode, a Pt wire as the counter electrode, and an Ag/AgCl electrode as the reference electrode. Impedance spectroscopy was performed using a 10 mV alternating current modulation amplitude at 0 V bias voltage. EIS measurements of the supporting electrode, without the membrane, were performed at the end of each experiment after the removal of the supported membrane via multiple rinses with copious amounts of detergent (2% Hellmanex III in DDW) and DDW, followed by buffer exchange to Tris-NaCl buffer. All measurements were performed in 10 mM Tris with 100 mM NaCl (pH 8).

## Fluorescence intensity and lifetime measurements of membrane potential

The fluorescence intensity and lifetime of the membrane dyes VF2.0.Cl and VF2.1.Cl was measured using a time-resolved imaging system based on an

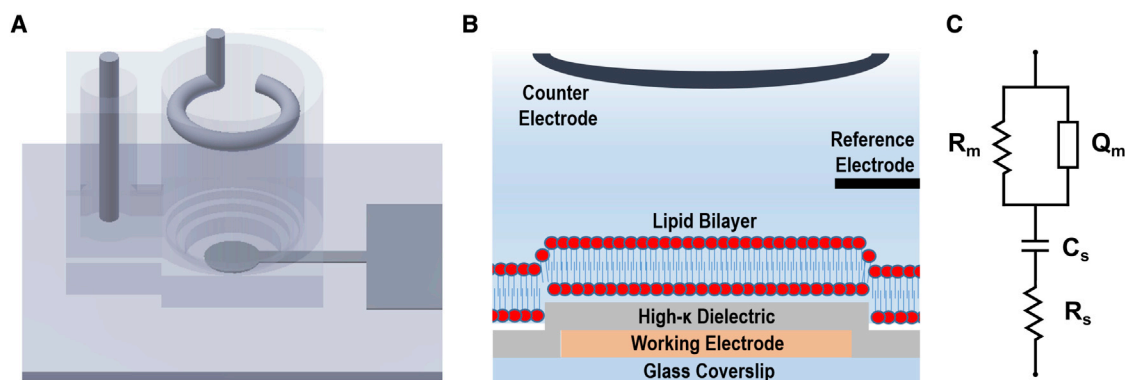


FIGURE 1 Electrically and optically addressable solid-supported lipid bilayer. (A) An electrochemical chamber is placed on top of a semitransparent Ti/Ta<sub>2</sub>O<sub>5</sub> electrode that supports the membrane. The chamber is filled with an electrolyte solution, and counter (Pt) and reference (Ag/AgCl) electrodes are positioned in the solution, forming a three-electrode cell. (B) A schematic drawing (not to scale) of the membrane and the underlying electrode support. (C) The electrical equivalent circuit model. The substrate is represented by the resistance of the semitransparent conducting layer and the electrolyte solution  $R_s$  and the capacitance of the insulating layer  $C_s$ . The membrane is approximated by a resistive element  $R_m$  connected in parallel to a constant phase element  $Q_m$ . To see this figure in color, go online.

inverted microscope (IX83; Olympus, Tokyo, Japan) coupled to a 60 $\times$  water-immersion objective (UPLSAPO60XW; Olympus). A light-emitting diode light source (SPECTRA X; Lumencor, Beaverton, OR) and a sCMOS camera (ORCA-Flash4.0 V3; Hamamatsu, Tokyo, Japan) were used for epifluorescence imaging. Time-resolved confocal fluorescence detection was performed in a time-correlated time-tagged recording mode using a 470 nm pulsed diode laser (LDH-D-C-470; PicoQuant, Berlin, Germany). The emitted light was collected and focused using a 180 mm lens (AC508-180-A, Thorlabs, Newton, NJ) into a 150  $\mu$ m pinhole ( $\sim$ 9 Airy units) at the conjugate image plane, and then collected and focused onto an avalanche photodiode detector (SPCM-AQRH-43-TR; Excelitas Technologies, Waltham, MA). The detector and the laser driver (PDL 800-D; PicoQuant) were connected to a time-correlated single-photon counting card (TimeHarp 260 PICO; PicoQuant). A data acquisition (DAQ) device (NI USB-6356; National Instruments, Austin, TX), controlled by home-written software (LabVIEW; National Instruments), was used for synchronizing the potentiostat and the time-correlated single-photon counting electronics. Lifetime curve fitting was performed using the maximum likelihood estimation method (52) with a model function of the form  $\exp(-t/\tau)$  for monoexponential decay and  $\sim \exp(-t/\tau_1) + R_0 \exp(-t/\tau_2)$  for biexponential decay, with an added constant background noise with a uniform probability distribution. Since the instrument response function of the described system was both temporally unstable and relatively long ( $\sim$ 310 ps), the fitting procedure was performed on the decaying tail of the fluorescence lifetime curve.

## RESULTS AND DISCUSSION

### Membrane-supporting metal-insulator substrate

An overall negatively charged lipid bilayer composed from a mixture of POPC and POPS phospholipids in a 4:1 molar ratio was formed on top of a Ti/Ta<sub>2</sub>O<sub>5</sub> electrode (Fig. 1), as described in [Materials and methods](#). Metal-oxide surfaces provide several key advantages as solid support for artificial lipid bilayers compared with purely conductive surfaces. First, faradic currents at the metal-liquid interface can induce electrochemical reactions with toxic products (53), which are significantly reduced once the conductive layer is passivated by an inert oxide layer. Second, when using fluorescent probes, an oxide layer reduces their undesired quenching due to energy transfer to surface plasmons in the metal layer (49,54). Ta<sub>2</sub>O<sub>5</sub> was chosen to serve as the insulating layer due to its relatively high (above 20) dielectric constant, high breakdown threshold, low leakage current, chemical stability, and biocompatibility (55,56). The nanoscale roughness of the solid support has a significant effect on the structural and dynamical properties of the SLB. The homogeneity of the bilayer film and the liquid-phase diffusional properties are related to the underlying substrate's physical and chemical properties (57). Even the surface treatment used before the deposition of the lipid membrane greatly affects membrane fluidity (58). Since lipid membranes are 4–5 nm in thickness, the supporting substrate roughness is a crucial parameter (12), which must be minimized to a sub-nm scale to achieve a complete and homogeneous lipid bilayer film. While ITO is routinely used for semitransparent conducting electrodes,

its nanoscale roughness ( $>$ 1 nm) limits the homogenous coverage of fluid lipid bilayers (23). Following a screening of different possible conducting layers, we chose a thin layer ( $\sim$ 8 nm) of Ti as the semitransparent conductive layer due to its low roughness and good adhesion to glass and to the upper Ta<sub>2</sub>O<sub>5</sub> layer. The surface roughness of the Ti/Ta<sub>2</sub>O<sub>5</sub> electrode surface was characterized with AFM and measured to be below 0.5 nm (Fig. S2 A). Since the phase transition temperatures of both POPC and POPS are below room temperature, the supported membrane is expected to be in a fluid phase, displaying translational diffusion of the constituting lipids. Therefore, fluorescence recovery after photobleaching was confirmed at several locations of each supported bilayer under study to ensure homogenous membrane preparations (Fig. S2 B).

### Electrical modeling and characterization of the supported membrane

The electrical properties of the lipid bilayer were characterized using EIS, an alternating current technique that is commonly used to measure the frequency-dependent complex impedance of electrochemical systems. Although these measurements are relatively straightforward, the interpretation of impedance spectra and the equivalent model circuit are challenging due to the complicated nature of real systems and the ambiguity in their multivariable description. Importantly, one needs to ascribe a physical meaning or purpose to each electrical element of the equivalent model circuit.

The metal-insulator-electrolyte system can be approximately modeled as a serially connected ideal resistor  $R_s$ , representing both the solution and substrate resistance, and capacitor  $C_s$ , representing the insulating layer (Figs. 2 and S3 C). We note that the electrical double layer at the oxide-electrolyte interface, commonly described as a combination of an immobile Stern layer and a mobile diffusive layer by the Gouy-Chapman-Stern model, is usually required for a complete description of electrode-electrolyte interfaces. These models require at least one ad hoc constant phase element (CPE). However, since the electrical double layer capacitance ranges between 6 and 12  $\mu$ F cm<sup>-2</sup> at the relevant electrolyte concentrations (59), higher than the capacitance of both the insulating layer and the membrane, its spectral contribution occurs at frequencies lower than the range described here. The impedance spectra of Ti/Ta<sub>2</sub>O<sub>5</sub> electrodes with varying thicknesses of the insulating layer are shown in Fig. S3.

Several experimental studies showed that, while SLBs commonly have a capacitance of 0.5–1  $\mu$ F cm<sup>-2</sup> (20,21,28), as would be theoretically expected for a typical layer of a lipid bilayer, membrane resistance greatly varies between different membrane compositions, substrates, and

preparation methods, ranging between  $10^4$  and  $10^7 \Omega \text{ cm}^2$ . In comparison, suspended (black) planar lipid bilayers possess similar capacitance yet considerably higher resistance ( $10^6$  to  $10^8 \Omega \text{ cm}^2$ ) (60). The lower resistance of SLBs can be understood as the result of inhomogeneities and defects in such large area membranes, which are considerably more physically stable compared with bilayers suspended in a liquid phase, and hence can tolerate structural imperfections.

Although channel-free membranes are commonly characterized by simple resistive and capacitive elements, the electric response of experimental realizations of these membranes does not exactly follow this ideal model. The description of homogenous planar bilayers is complicated due to the complex microscopic nature of the lipid bilayer, its two interfaces with the surrounding electrolyte, and the submembrane electrolyte reservoir between the solid support and the lipid bilayer (21,61). Although the internal structure of membranes and the dielectric properties of each of its components can be modeled as an elaborate equivalent circuit, it is hard to unambiguously distinguish the contribution of each component to the EIS spectra (21,62,63). Alternatively, the capacitive element describing the membrane can be generalized with a CPE (21,64,65), with an impedance of the form  $Z_Q(\omega) = \frac{1}{Q_m(i\omega)^n}$ , where  $\omega$  is the angular frequency, and  $Q_m$  and  $n$  are frequency-independent coefficients. As  $n$  approaches the value of 1,  $Z_Q(\omega)$  approximates an ideal capacitor. One should note that such a heuristic element lacks a concrete physical meaning. Moreover, they are, in principle, inadequate for the description of surface inhomogeneity and defects, for which more elaborate electrical network models are required (61,66). While the simplified electrical model presented here serves well in interpreting the response of voltage-sensitive membrane dyes to SLB transmembrane polarization, a more detailed microscopic model of the electrostatic potential profile across the membrane and its interfaces is needed to fully describe electrostatic effects influencing membrane organization and membrane protein conformational changes. Measurements of these microscopic electrostatic potentials can be performed, for example, by interference (67) and fluorescence (68,69) microscopies, Kelvin probe force microscopy (70), scanning ion conductance microscopy (71), or DNA origami sensors (72). In addition, the effect of different lipid headgroups and chains on the microscopic electric potential can be investigated by modeling the electrochemical system with a more elaborate equivalent electrical circuit of the membrane (21) and the electrical double layer (59), and performing comparative EIS studies for SLBs of different lipid compositions.

As shown in Fig. 1 C, we model the electrical response of the system by assuming an overall impedance of the form  $Z(\omega) = Z_s(\omega) + Z_m(\omega)$ , where  $Z_s(\omega)$  is the imped-

ance associated with the substrate and electrolyte solution, and  $Z_m(\omega)$  is the impedance associated with the lipid bilayer. The main contributors to  $Z_s(\omega)$  are the supporting substrate sheet resistance together with the small contribution from the resistance of the electrolyte solution  $R_s$ , and the capacitance of the insulating oxide layer  $C_s$ . Therefore, the impedance of the supporting substrate can be approximated to  $Z_s(\omega) = R_s + \frac{1}{i\omega C_s}$ . The impedance of the membrane is approximated by a resistive element  $R_m$  connected in parallel with a CPE  $Z_Q(\omega) = \frac{1}{Q_m(i\omega)^n}$ , resulting in a total membrane impedance of the form  $Z_m(\omega) = \frac{R_m Z_Q(\omega)}{R_m + Z_Q(\omega)}$ . Fig. 2 shows the impedance spectra and the best fit of the equivalent circuit models, before and after bilayer formation, of two distinct representative preparations, differing mainly by their membrane resistance  $R_m$ . The preparations of both the high  $R_m$  and low  $R_m$  membranes were identical, with the high  $R_m$  sample allowed for an additional stabilization time after membrane formation and before the staining procedure, as described in Materials and methods. As will be shown, the electrical parameters describing the substrate and the membrane dictate the resulting magnitude and dynamics of the voltage drop on the membrane.

### Supported membrane electrical polarization dynamics

The voltage drop on the membrane, the transmembrane potential, can be modeled by considering the electrical circuit dynamics of the equivalent circuit and the corresponding fitted parameters (Fig. 2). In the frequency domain, for an overall voltage drop  $V(\omega)$  on the system, the voltage drop on the membrane would be:

$$V_m(\omega) = \left( \frac{Z_s(\omega)}{Z_m(\omega)} + 1 \right)^{-1} V(\omega). \quad (1)$$

Assuming ideal resistive and capacitive components, with a constant membrane capacitance  $C_m$  (thus a capacitive element impedance  $Z_Q(\omega) = \frac{1}{i\omega C_m}$ ), the voltage drop upon the substrate  $V_s$  and the membrane  $V_m$  follow simple dynamical equations:

$$\frac{dV_s}{dt} = \frac{1}{R_s C_s} [V - V_s - V_m], \quad (2)$$

$$\frac{dV_m}{dt} = \frac{1}{C_m} \left[ \frac{1}{R_s} (V - V_s - V_m) - \frac{V_m}{R_m} \right], \quad (3)$$

where  $V$  is the time-dependent voltage drop on the whole circuit. Assuming the total voltage drop on the system is switched abruptly from 0 to  $V_0$  at  $t = 0$ , the step response of the potential drop on the membrane is

$$V_m(t) = \frac{2R_m C_s V_0}{\sqrt{(\tau_s + \tau_m + R_m C_s)^2 - 4\tau_s \tau_m}} \exp\left(-\frac{\tau_s + \tau_m + R_m C_s}{2\tau_s \tau_m} t\right) \times \sinh\left(\frac{\sqrt{(\tau_s + \tau_m + R_m C_s)^2 - 4\tau_s \tau_m}}{2\tau_s \tau_m} t\right), \quad (4)$$

where  $\tau_m = R_m C_m$  and  $\tau_s = R_s C_s$  are the time constant arising from the (parallel RC) membrane and (serial RC) substrate electrical properties, respectively. As experimentally shown in the following section using optical measurements

of the membrane potential, after a rapid initial rising period, the potential drop on the membrane decays exponentially as  $\sim \exp\left(-\frac{\tau_s + \tau_m + R_m C_s - \sqrt{(\tau_s + \tau_m + R_m C_s)^2 - 4\tau_s \tau_m}}{2\tau_s \tau_m} t\right)$ .

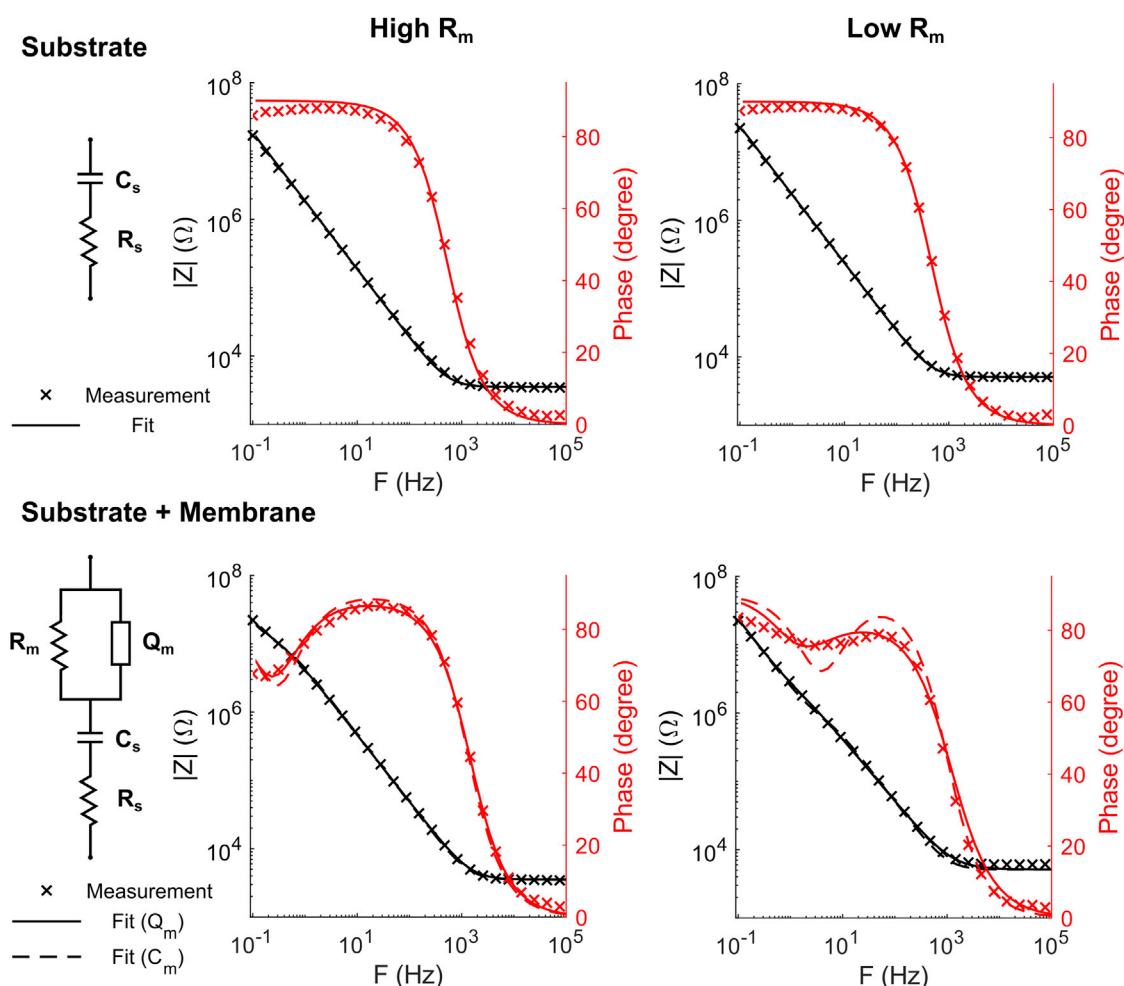


FIGURE 2 Electrical characterization of the supported membrane via electrochemical impedance spectroscopy. The complex impedance spectra (amplitude and phase) of a bare Ti/Ta<sub>2</sub>O<sub>5</sub> substrate (*top*) and the same substrate supporting a lipid bilayer (*bottom*) are shown for two distinct membrane preparations, differentiated mainly by the time they were allowed to relax on the substrate after membrane formation, resulting in different membrane resistance  $R_m$ . The left panel shows the equivalent circuit used in modeling the impedance spectra. The bare electrode is modeled by a simple resistive element  $R_s$  in series with a capacitive element  $C_s$ , and the membrane is approximated by a resistive element  $R_m$  in parallel with a constant phase element  $Q_m$ . The best fit of each impedance spectra is shown for both a general constant phase element (*solid line*), and the ideal case ( $n = 1$ ), representing a simple capacitive element  $Z_Q(\omega) = \frac{1}{i\omega C_m}$  (*dashed line*). The fitted parameters of the bare substrate model were used as fixed parameters for the fitting of the supported membrane. The best-fit parameters for the high  $R_m$  system are  $R_s = 249.4 \Omega \text{ cm}^2$ ,  $C_s = 1.2 \mu\text{F cm}^{-2}$  for the substrate, and  $R_m = 510.5 \text{ k}\Omega \text{ cm}^2$ ,  $Q_m = 0.95 \mu\text{F s}^{n-1} \text{ cm}^{-2}$ ,  $n = 0.96$ , or  $R_m = 457.9 \text{ k}\Omega \text{ cm}^2$ ,  $C_m = 0.79 \mu\text{F cm}^{-2}$  for the membrane. The best-fit parameters for the low  $R_m$  system are  $R_s = 359.9 \Omega \text{ cm}^2$ ,  $C_s = 0.95 \mu\text{F cm}^{-2}$  for the substrate, and  $R_m = 63.9 \text{ k}\Omega \text{ cm}^2$ ,  $Q_m = 2.1 \mu\text{F s}^{n-1} \text{ cm}^{-2}$ ,  $n = 0.85$  or  $R_m = 33.2 \text{ k}\Omega \text{ cm}^2$ ,  $C_m = 0.84 \mu\text{F cm}^{-2}$  for the membrane. To see this figure in color, go online.

The decay of the membrane potential occurs due to the finite resistance of the membrane, which causes the voltage drop across the membrane to decrease, while the voltage drop across the insulating substrate increases and eventually approaches the value of the total voltage drop applied on the system. For the case of an infinitely resistive membrane, the potential drop on the membrane behaves as a simple charging capacitor  $V_m(t) = \frac{C_s V_0}{C_m + C_s} \left[ 1 - \exp\left(-\frac{C_m + C_s}{C_m} \frac{t}{\tau_s}\right) \right]$ , displaying no leakage of the membrane potential following its charging, with the total voltage drop shared between the membrane and the insulating substrate according to their capacitance values.

### Optical observation of membrane polarization

To demonstrate the ability to control the transmembrane voltage of the SLB, we used optical voltage-sensitive membrane dyes as an orthogonal measurement approach. Over the past five decades, a wide array of membrane potential in-

dicators has been developed and applied for various biological membranes (73–76). These optical indicators incorporate into the lipid bilayer, and display voltage-dependent optical properties, such as absorption and fluorescence. Here, we used VoltageFluor (VF) (77), a membrane dye that utilizes voltage-dependent photoinduced electron transfer between an electron donor and a fluorescent acceptor through a molecular wire (Fig. 3 A). Specifically, we monitored the membrane potential of the electrically accessible supported membrane with VF2.1.Cl (77,78), a VF derivative with a biexponential fluorescence decay curve that displays both intensity and lifetime changes upon changes in transmembrane potential. As a control, we used a similar derivative of the dye, VF2.0.Cl, which is spectrally similar to VF2.1.Cl but, however, lacks the electron-rich donor and therefore acts as a voltage-insensitive membrane dye (79). Fig. 3 shows the fluorescence intensity and lifetime response of VF2.0.Cl and VF2.1.Cl upon electrical polarization of the supported membrane stained with 100 nM of either dye, using the high  $R_m$  membrane described in Fig. 2. To label only the leaflet closer to the

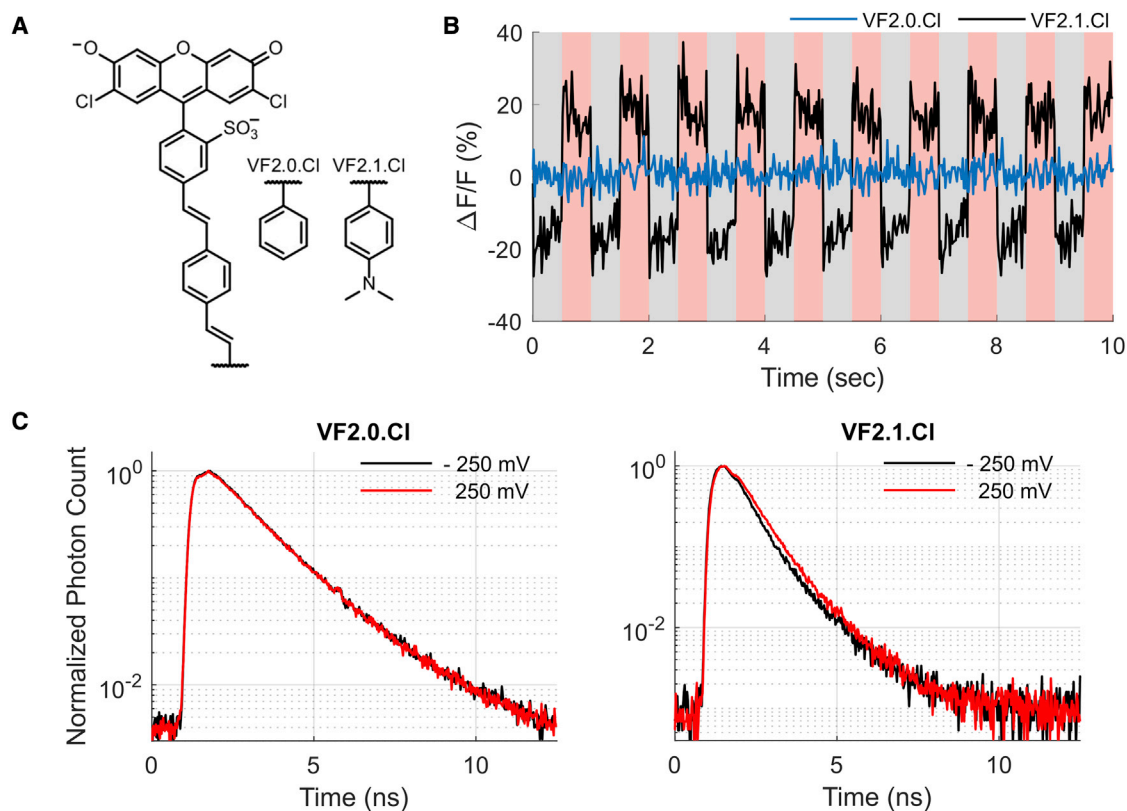


FIGURE 3 Optical monitoring of changes in membrane potential. (A) Structure of the two VF membrane dyes used in this study. Both dyes are composed of a fluorophore conjugated to a molecular wire, with (VF2.1.Cl) or without (VF2.0.Cl) an electron-rich aniline donor, rendering the dyes to be either voltage sensitive or insensitive, respectively. (B) The fluorescence emission intensity of a voltage-sensitive (VF2.1.Cl, black) and a voltage-insensitive (VF2.0.Cl, blue) membrane dye upon electrical polarization of the stained membrane. The total voltage drop upon the electrochemical system was alternated between  $-250$  mV (gray-shaded area) and  $+250$  mV (red-shaded area). Fluorescence intensity traces were calculated by binning the overall detected photon arrivals at 20 ms time bins. Time-resolved photon detection was used to measure the fluorescence lifetime decay of both dyes at each applied voltage. (C) shows the fluorescence decay curves of both dyes at a voltage drop of  $-250$  mV (black) and  $250$  mV (red), averaged over 30 polarization cycles, demonstrating the lifetime response of VF2.1.Cl to changes in membrane potential. To see this figure in color, go online.

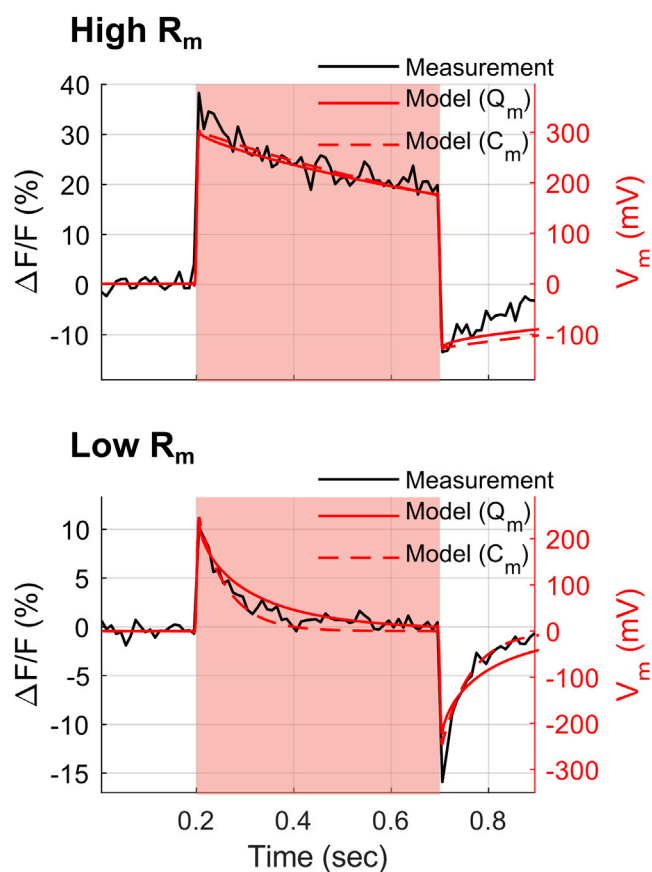


FIGURE 4 Optical monitoring of membrane potential dynamics. The averaged fluorescence emission intensity (*black*) change upon a pulsed polarization from 0 to +500 mV (*red-shaded area*) of the high (*upper panel*) and low (*lower panel*) resistance membranes shown in Fig. 2, averaged over 20 polarization cycles. The expected response to such polarization pulse is calculated by solving the dynamical equations of the equivalent circuit model of the membrane, using the best-fit parameters described in Fig. 2, assuming the change in transmembrane potential follows the voltage drop on the membrane  $V_m(t)$ . The calculated behavior of the membrane potential  $V_m(t)$  upon electric polarization is shown for a membrane modeled both with a constant phase element  $Q_m$  (*solid red*) and an ideal capacitive element  $C_m$  (*dashed red*). To see this figure in color, go online.

bulk electrolyte, staining was performed externally for 5 min on a fully formed membrane, followed by 10 rounds of buffer exchange to remove excess dye from the bath solution. All potentials were applied versus the Ag/AgCl electrode. Before each measurement, the detected region was photobleached, thus only the fluorescence of latterly diffusing dye molecules was measured. The absence of voltage-dependent changes in fluorescence of VF2.0.Cl implies that the voltage-dependent response of VF2.1.Cl can be attributed to changes in the directional transmembrane potential, and not to other artifacts, such as local change of ion concentrations upon polarization of the working electrode. The change in fluorescence intensity of VF2.1.Cl upon a total applied polarization of 500 mV was measured to be  $\Delta F/F \approx 47 \pm 1.3\%$ , averaged over 30 polarization cycles at three regions of the supported membrane. The

fluorescence amplitude-averaged lifetime showed an increase from  $0.64 \pm 0.03$  ns at  $-250$  mV to  $0.70 \pm 0.02$  ns at  $250$  mV, corresponding to a relative change of  $\Delta\tau/\tau \approx 10 \pm 4.1\%$  upon a total applied polarization of 500 mV.

As discussed in the previous section, one should note that the voltage drop across the membrane (the transmembrane potential) is necessarily smaller than the overall applied voltage, since the overall voltage drop is distributed among the different electrical components constituting the electrochemical system. Figs. S4 and 4 show the fluorescence intensity trajectories and the averaged responses, respectively, to pulsed electrical polarization of VF2.1.Cl in both the high and low  $R_m$  membranes characterized in Fig. 2. As discussed in the previous section, both the magnitude and dynamics of the voltage drop on the membrane are highly dependent on the electrical properties of the metal-insulator-bilayer system. In particular, the membrane resistance  $R_m$ , which significantly varies between preparation methods of the lipid bilayer, dictates to a great extent the leakage of membrane potential to the substrate over time. The substrate capacitance  $C_s$ , which is controlled by the fabrication process, has to be as large as possible to increase the actual voltage drop on the membrane, as demonstrated in Fig. S5. The predicted membrane potential magnitude and dynamics can be calculated using Eqs. 1–3, using the fitted parameters of the equivalent circuit. Since the CPE exponent  $n$  is close to 1, as shown in Fig. 2, the more complex CPE description is approximated well by an ideal capacitive element. Hence, as shown in Fig. 4, the simplified model, in which the membrane is modeled by ideal resistive and capacitive components, is in good agreement with the optically observed membrane electric polarization.

For the high  $R_m$  membrane demonstrated in Figs. 2 and 3, assuming the membrane potential step response described in Eq. 4, a total voltage drop of 500 mV results in membrane polarization of approximately 300 mV at its peak. Even after accounting for the smaller membrane voltage drop due to circuit dynamics, the measured optical response to changes in membrane potential is smaller than previously published results from patch-clamped cells stained with VF2.1.Cl. In HEK293T cells, the change in fluorescence intensity of VF2.1.Cl was measured to be  $\Delta F/F \approx 27\%$  per 100 mV, and the fluorescence lifetime showed a sensitivity of  $3.5 \pm 0.08$  ps/mV and a lifetime of  $1.77 \pm 0.02$  ns at 0 mV, corresponding to a relative change of  $\Delta\tau/\tau \approx 22.4 \pm 0.4\%$  per 100 mV (77,78). This discrepancy can be attributed to several factors. Since the interface and environment on both sides of the supported membrane are highly asymmetrical, assigning one value for the transmembrane potential may be an oversimplification. For example, one could test and compare the optical response of voltage-sensitive membrane dyes in each of the bilayer leaflets, or increase the electrolyte reservoir underneath the membrane by distancing the bilayer from the solid support (19,30,80).

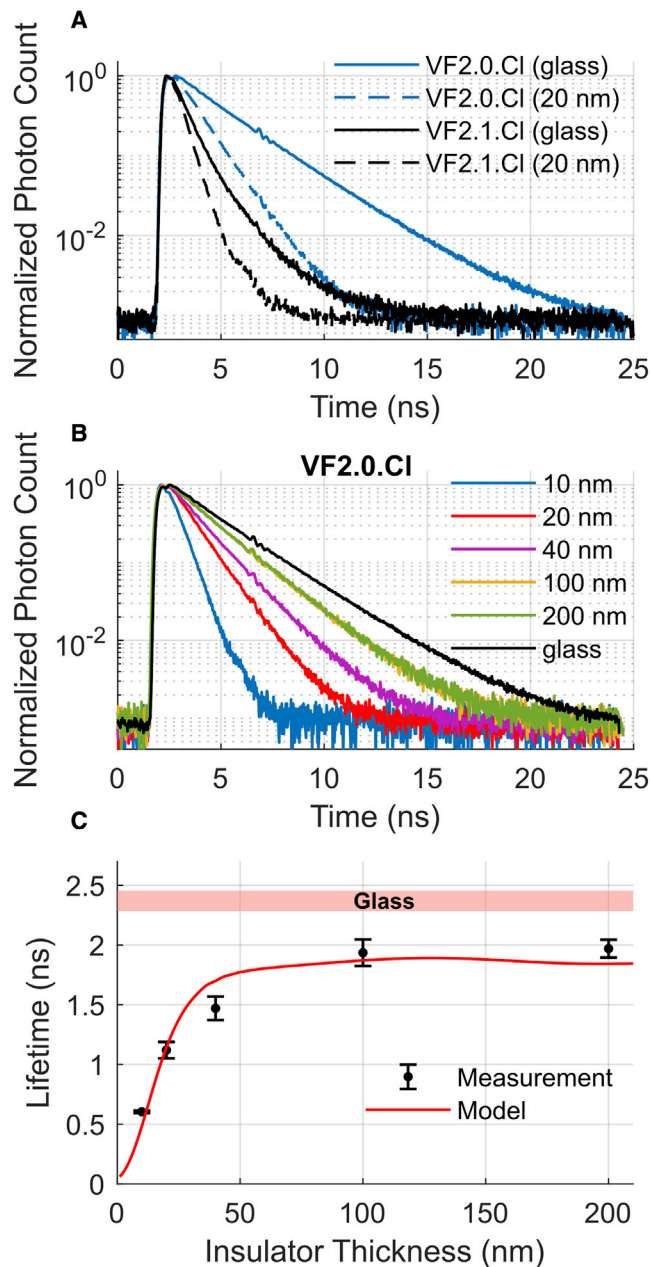


**FIGURE 5** The influence of MIET on the fluorescence lifetime decay. (A) The lifetime decay curves of VF2.0.Cl (blue) and VF2.1.Cl (black), staining a membrane supported by a glass (solid line) or Ti/Ta<sub>2</sub>O<sub>5</sub> (dashed line) substrate, with a 20 nm insulating layer of Ta<sub>2</sub>O<sub>5</sub>. (B) The lifetime decay curves of VF2.0.Cl supported by Ti/Ta<sub>2</sub>O<sub>5</sub> substrates with varying thicknesses of the insulating layer Ta<sub>2</sub>O<sub>5</sub>. The lifetime decay constant for each insulating layer thickness, averaged over five different regions of the membrane, are shown in (C) (black), with error bars representing the standard deviation of the fitted decay constants. The red-shaded area indicates the lifetime distribution of VF2.0.Cl in a membrane supported on bare glass. The theoretically calculated dependence of the fluorescence lifetime on the insulator thickness (red) is shown for the case of an emission dipole that is oriented at an angle of 35° relative to the membrane plane, assuming a quantum yield of 0.3, a free space lifetime of 2.27 ns and optical layer parameters as described in Table S1. To see this figure in color, go online.

Another important consideration should be the effect of the conducting layer on the fluorescence of the optical probe. In particular, MIET (49,81) increases the radiative transition rate of the fluorophore as the fluorophore gets closer to the conducting layer, resulting in a shorter lifetime. Fig. 5 A shows the lifetime of VF2.0.Cl and VF2.1.Cl in membranes supported on glass and the Ti/Ta<sub>2</sub>O<sub>5</sub> substrate used for the measurements described above. The lifetime of the monoexponential VF2.0.Cl reduced from  $2.40 \pm 0.08$  to  $1.12 \pm 0.07$  ns for membranes supported on glass and the Ti/Ta<sub>2</sub>O<sub>5</sub> substrate, respectively. The biexponential decay curve VF2.1.Cl, which has an amplitude-averaged lifetime of  $0.78 \pm 0.04$  ns for membranes supported on glass, reduced to  $0.48 \pm 0.003$  ns when supported by the Ti/Ta<sub>2</sub>O<sub>5</sub> substrate. However, the lifetime of VF2.1.Cl on the same substrate was measured to be  $0.67 \pm 0.02$  ns once the Ti/Ta<sub>2</sub>O<sub>5</sub> substrate was electrically connected to the potentiostat and the total voltage drop on the system was set to 0 mV. A possible explanation for the difference of the fluorescence decay between the two measurements is the native surface potential of the electrode-membrane system, which is different from the case where the system is electrically set to a constant overall potential of 0 mV. The dependence of the fluorescence lifetime on the distance between the membrane dye and the conducting Ti layer was theoretically modeled for VF2.0.Cl, which has a simpler monoexponential decay curve. Fig. 5 B shows the fluorescence decay curve of VF2.0.Cl in membrane supported on a Ti/Ta<sub>2</sub>O<sub>5</sub> substrate with varying thicknesses of the insulating layer Ta<sub>2</sub>O<sub>5</sub>, displaying the shortening of the fluorescence lifetime due to MIET as the membrane dye is closer to the conductive layer. Fig. 5 C shows the fitted fluorescence decay constant for each decay curve, along with the theoretically calculated lifetime for a model emission dipole (82,83). To theoretically calculate the dependence of the fluorescence lifetime on the insulator thickness, one needs to know the complex-valued refractive indices of all layers surrounding the emission dipole, together with its orientation, free space fluorescence lifetime, and quantum yield. Here, we assumed that the emission dipole is oriented at an angle of 35° relative to the membrane plane, as estimated by molecular dynamics simulations of a similar membrane dye (84). We note that the discrepancy between the measurement and the theoretical model cannot be explained merely as the result of inaccurate knowledge of emission dipole, as was checked by altering these fluorophore-dependent parameters in the model calculations. A possible explanation could be that the assumed imaginary part of the refractive index of the conducting layer is inaccurate, which would greatly change the dependence of the fluorescence lifetime on the distance to the conducting layer. Here, we measured the complex-valued refractive indices of layers with ellipsometry, treating the Ti layer as a single homogenous layer with an effective refractive index (Table S1). However, as shown in Fig. S3 A, the ~8 nm Ti layer displays a

nonuniform electron density, most likely due to the consecutive Ta<sub>2</sub>O<sub>5</sub> deposition. This nonhomogeneity may cause the optical properties of the Ti layer to differ from the ones assumed in the model, and therefore alter the effect of MIET on the fluorescence lifetime.

The lifetime dependence of the fluorescent probe on its distance from the conducting layer can be utilized to measure its axial location with sub-nm resolution (85), as discussed in the following section. In addition, one should take this change in radiative transition rate into account when considering quantitative optical measurements based on fluorescent quenching, such as Förster resonance energy transfer (FRET) or photoinduced electron transfer. The exact nature of this effect will depend upon the complete description of electronic transitions from the photoexcited state. For example, we consider a simple model in which a photoexcited state relaxes either radiatively or nonradiatively with a total de-excitation transition rate of  $k_T = k_R(z) + k_{NR} + k_{ET}(V)$ , where  $k_R(z)$  is the radiative rate, which depends upon the distance of the fluorophore from the conducting surface,  $k_{NR}$  is the nonradiative relaxation rate, and  $k_{ET}(V)$  is a voltage-dependent electron transfer rate to a charged-separated state, assuming the charge-separated state relaxes nonradiatively (86). The average emission intensity  $F$  of such fluorophore is proportional to its quantum yield, i.e.,  $k_R(z)/k_T$ . The relative change in fluorescent emission due to small changes in the applied voltage is  $\Delta F/F = -\Delta k_{ET}(V)/k_T$ , where  $\Delta k_{ET}(V)$  is the corresponding change in the electron transfer transition rate  $k_{ET}(V)$  as a function of applied voltage. Therefore, an increased radiative transition rate, such as in the case of MIET, inevitably reduces the sensitivity of such optical probes to changes in membrane potential.

## Possible applications

### *Optical investigation of voltage-dependent molecular dynamics*

Fluorescence microscopy and spectroscopy are frequently used in the study of membranes and their associated proteins. In particular, FRET provides a powerful approach for nanoscale measurements of molecular structure and dynamics of biomolecules such as DNA, RNA, proteins, and their interaction (87–91). While FRET allows for the measurement of the distance between donor and acceptor molecules, MIET allows for nanoscale axial localization of fluorescent probes above the conducting substrate (48,49). In particular, using graphene as the conducting substrate results in significant dependence of the fluorescence lifetime to sub-nm changes in the axial direction (85,92), making this method highly relevant for the study of membrane proteins. Applying optical techniques, such as FRET and MIET, utilizing the platform described in this work can allow for novel experiments that probe voltage-induced molecular dynamics of membrane proteins. Beyond voltage-gated ion channels, this experi-

mental approach could be used to investigate the role of membrane potential and electrostatics in the conformation of membrane proteins (43–46). In addition to membrane and protein biophysics, combining optical and electrochemical tools can be used for studying the physicochemical properties of solid-electrolyte interfaces. Such studies were performed using electrochemiluminescence (93,94) and electric-double-layer-modulation (95) microscopies, as well as many other optical techniques (96). In addition to fluorescence microscopy of fluorescent probes that are inherently environment-sensitive, applying ultrasensitive methods, such as FRET and MIET, with probes that are electrically responsive due to their net charge can allow for the study of interfaces at a sub-nm resolution.

### *Biologically relevant model membranes*

Although synthetic lipid bilayers, such as the ones prepared in this work, provide a clean and robust experimental system, they fail to mimic important features of real biological membranes, which contain a rich complexity of biological membranes, such as different phospholipid headgroups, saturation levels of their tails, membrane proteins, cholesterol, and carbohydrates (97). Such realistic membranes will include lateral inhomogeneities and macroscopic and nanoscopic domains of different membrane fluidity and phase. More biologically relevant membranes can be achieved by either additional synthetic (98) or biologically derived components (99), or by extracting the components from real cell membranes by induced extracellular vesicles (100). One should note that the addition of foreign components to the bilayer film, such as labeled fluorescent probes, can affect the overall functional properties of the membrane (101). Hence, low probe concentrations and proper control experiments should be considered when adding extrinsic fluorescent probes. In addition, enhanced membrane stability and better incorporation of membrane proteins can be achieved through the introduction of a polymer cushion layer or a tethering layer that anchors one leaflet to the substrate (16,17,102–104). Similar to the work shown here, these tethered membranes can also be electrochemically characterized when deposited on a conductive substrate (61,105–107).

## CONCLUSION

Combining both electrochemical and optical tools for studies that utilize SLBs offer novel possibilities for voltage-dependent investigations of membranes and their associated biomolecules. While electrochemical tools allow for electrical characterization and control of the membrane and the supporting substrate, optical measurements offer an orthogonal approach for probing membranes, membrane proteins, and their dependence on external signals. In this work, we establish an electrochemical-optical platform for SLBs and demonstrate electrical control of the membrane

potential by independently monitoring it with voltage-sensitive dyes. We show that the membrane potential is governed by the circuit dynamics of the electrochemical system, which can be understood by its characterization via EIS. In addition, we demonstrate that the conducting electrode layer affects the fluorescent emission of the optical probe through MIET and discuss possible resulting implications. Such electrically and optically addressable membranes can provide a platform for a vast array of ensemble and single-molecule optical methods for the study of folding and interaction of membrane proteins.

## DATA AVAILABILITY

Raw data of all EIS, imaging, and time-resolved fluorescence measurements presented in this work is available at Zenodo: <https://doi.org/10.5281/zenodo.5769883>. Home-written code (MATLAB) for the analysis shown in this work is available upon request.

## SUPPORTING MATERIAL

Supporting material can be found online at <https://doi.org/10.1016/j.bpj.2022.05.037>.

## AUTHOR CONTRIBUTIONS

S.Y. prepared the samples and performed optical and electrochemical experiments. A.M. prepared the vesicles. J.K. fabricated the metal-insulator electrodes. E.T. performed AFM for surface characterization. T.C. and J.E. analyzed the MIET data. E.W.M. provided the membrane dyes. S.Y. and S.W. designed and planned the study. All co-authors participated in writing the manuscript.

## ACKNOWLEDGMENTS

We thank Dr. Shay Tirosh and Prof. Arie Zaban for potentiostat instrument access and help with EIS, Dr. Maria Tkachev and Dr. Ilana Perelshtein for performing cross-sectional HR-TEM imaging of the electrode, Dr. Ayelet Atkins for performing cryo-EM imaging of the vesicles, and Mark Oksman for performing ellipsometry measurements. This work has received funding from the European Research Council (ERC) under the European Union's Horizon 2020 research and innovation program under grant agreement no. 669941, by the Human Frontier Science Program (HFSP) research grant RGP0061/2015, by the BER program of the Department of Energy Office of Science grant DE-SC0020338, by the STROBE National Science Foundation Science & Technology Center, grant no. DMR-1548924, by the Israel Science Foundation (ISF) grant 813/19, and by the Bar-Ilan Research & Development Co, the Israel Innovation Authority, grant no. 63392.

## DECLARATION OF INTERESTS

The authors declare no competing interests.

## REFERENCES

- Tamm, L. K., and H. M. McConnell. 1985. Supported phospholipid bilayers. *Biophys. J.* 47:105–113. [https://doi.org/10.1016/s0006-3495\(85\)83882-0](https://doi.org/10.1016/s0006-3495(85)83882-0).
- Sackmann, E. 1996. Supported membranes: scientific and practical applications. *Science*. 271:43–48. <https://doi.org/10.1126/science.271.5245.43>.
- Castellana, E. T., and P. S. Cremer. 2006. Solid supported lipid bilayers: from biophysical studies to sensor design. *Surf. Sci. Rep.* 61:429–444. <https://doi.org/10.1016/j.surfrep.2006.06.001>.
- Andersson, J., P. Bilotto, ..., W. Knoll. 2020. Solid-supported lipid bilayers – a versatile tool for the structural and functional characterization of membrane proteins. *Methods*. 180:56–68. <https://doi.org/10.1016/j.ymeth.2020.09.005>.
- Groves, J. T., and M. L. Dustin. 2003. Supported planar bilayers in studies on immune cell adhesion and communication. *J. Immunol. Methods*. 278:19–32. [https://doi.org/10.1016/s0022-1759\(03\)00193-5](https://doi.org/10.1016/s0022-1759(03)00193-5).
- Blodgett, K. B. 1935. Films built by depositing successive monomolecular layers on a solid surface. *J. Am. Chem. Soc.* 57:1007–1022. <https://doi.org/10.1021/ja01309a011>.
- Kurniawan, J., J. F. Ventrici de Souza, ..., T. L. Kuhl. 2018. Preparation and characterization of solid-supported lipid bilayers formed by Langmuir–blodgett deposition: a tutorial. *Langmuir*. 34:15622–15639. <https://doi.org/10.1021/acs.langmuir.8b03504>.
- Keller, C. A., K. Glasmästar, ..., B. Kasemo. 2000. Formation of supported membranes from vesicles. *Phys. Rev. Lett.* 84:5443–5446. <https://doi.org/10.1103/physrevlett.84.5443>.
- Zeineldin, R., J. A. Last, ..., G. P. Lopez. 2006. Using bicellar mixtures to form supported and suspended lipid bilayers on silicon chips. *Langmuir*. 22:8163–8168. <https://doi.org/10.1021/la060817r>.
- Ferhan, A. R., B. K. Yoon, ..., N. J. Cho. 2019. Solvent-assisted preparation of supported lipid bilayers. *Nat. Protoc.* 14:2091–2118. <https://doi.org/10.1038/s41596-019-0174-2>.
- Alessandrini, A., and P. Facci. 2014. Phase transitions in supported lipid bilayers studied by AFM. *Soft Matter*. 10:7145–7164. <https://doi.org/10.1039/c4sm01104j>.
- Blachon, F., F. Harb, ..., J. P. Rieu. 2017. Nanoroughness strongly impacts lipid mobility in supported membranes. *Langmuir*. 33:2444–2453. <https://doi.org/10.1021/acs.langmuir.6b03276>.
- Bayerl, T. M., and M. Bloom. 1990. Physical properties of single phospholipid bilayers adsorbed to micro glass beads. A new vesicular model system studied by 2H-nuclear magnetic resonance. *Biophys. J.* 58:357–362. [https://doi.org/10.1016/s0006-3495\(90\)82382-1](https://doi.org/10.1016/s0006-3495(90)82382-1).
- Johnson, S. J., T. Bayerl, ..., E. Sackmann. 1991. Structure of an adsorbed dimyristoylphosphatidylcholine bilayer measured with specular reflection of neutrons. *Biophys. J.* 59:289–294. [https://doi.org/10.1016/s0006-3495\(91\)82222-6](https://doi.org/10.1016/s0006-3495(91)82222-6).
- Nickel, B. 2008. Nanostructure of supported lipid bilayers in water. *Biointerphases*. 3:FC40–FC46. <https://doi.org/10.1116/1.3007998>.
- Wong, J. Y., C. K. Park, ..., J. Israelachvili. 1999. Polymer-Cushioned bilayers. II. An investigation of interaction forces and fusion using the surface forces apparatus. *Biophys. J.* 77:1458–1468. [https://doi.org/10.1016/s0006-3495\(99\)76993-6](https://doi.org/10.1016/s0006-3495(99)76993-6).
- Tanaka, M., and E. Sackmann. 2005. Polymer-supported membranes as models of the cell surface. *Nature*. 437:656–663. <https://doi.org/10.1038/nature04164>.
- Jackman, J. A., W. Knoll, and N.-J. Cho. 2012. Biotechnology applications of tethered lipid bilayer membranes. *Materials*. 5:2637–2657. <https://doi.org/10.3390/ma5122637>.
- Chung, M., R. D. Lowe, ..., S. G. Boxer. 2009. DNA-tethered membranes formed by giant vesicle rupture. *J. Struct. Biol.* 168:190–199. <https://doi.org/10.1016/j.jsb.2009.06.015>.
- Lin, J., M. Merzlyakov, ..., P. C. Se arson. 2008. Impedance spectroscopy of bilayer membranes on single crystal silicon. *Biointerphases*. 3:FA33–FA40. <https://doi.org/10.1116/1.2896117>.
- Wiegand, G., N. Arribas-Layton, ..., P. Wagner. 2002. Electrical properties of supported lipid bilayer membranes. *J. Phys. Chem. B*. 106:4245–4254. <https://doi.org/10.1021/jp014337e>.
- Purrucker, O., H. Hillebrandt, ..., M. Tanaka. 2001. Deposition of highly resistive lipid bilayer on silicon–silicon dioxide electrode

- and incorporation of gramicidin studied by ac impedance spectroscopy. *Electrochim. Acta.* 47:791–798. [https://doi.org/10.1016/s0013-4686\(01\)00759-9](https://doi.org/10.1016/s0013-4686(01)00759-9).
23. Hoyo, J., E. Gaus, ..., F. Sanz. 2013. Incorporation of ubiquinone in supported lipid bilayers on ITO. *J. Phys. Chem. B.* 117:7498–7506. <https://doi.org/10.1021/jp4004517>.
  24. Gritsch, S., P. Nollert, ..., E. Sackmann. 1998. Impedance spectroscopy of porin and gramicidin pores reconstituted into supported lipid bilayers on Indium–Tin-oxide electrodes. *Langmuir.* 14:3118–3125. <https://doi.org/10.1021/la9710381>.
  25. Gao, H., G. A. Luo, ..., H. Ti Tien. 2000. Fabrication and photoelectric properties of self-assembled bilayer lipid membranes on conducting glass. *J. Photochem. Photobiol. B Biol.* 59:87–91. [https://doi.org/10.1016/s1011-1344\(00\)00140-8](https://doi.org/10.1016/s1011-1344(00)00140-8).
  26. Sinner, A., and A. Offenhäuser. 1998. The electrical characterization of supported phospholipid bilayers using titanium/titanium oxide microelectrodes. *Thin Solid Films.* 327-329:758–761. [https://doi.org/10.1016/s0040-6090\(98\)00781-0](https://doi.org/10.1016/s0040-6090(98)00781-0).
  27. Briand, E., M. Zäch, ..., S. Petronis. 2010. Combined QCM-D and EIS study of supported lipid bilayer formation and interaction with pore-forming peptides. *Analyst.* 135:343–350. <https://doi.org/10.1039/b918288h>.
  28. Flynn, K. R., M. L. Ackland, and A. A. J. Torriero. 2018. Electrochemical impedance spectroscopy study of the interaction of supported lipid bilayers with free docosahexaenoic acid. *Med. Anal. Chem. Int. J. 2.* <https://doi.org/10.23880/macij-16000122>.
  29. Kawan, M., T. C. Hidalgo, ..., S. Inal. 2020. Monitoring supported lipid bilayers with n-type organic electrochemical transistors. *Mater. Horiz.* 7:2348–2358. <https://doi.org/10.1039/d0mh00548g>.
  30. Cornell, B. A., V. L. B. Braach-Maksvytis, ..., R. J. Pace. 1997. A biosensor that uses ion-channel switches. *Nature.* 387:580–583. <https://doi.org/10.1038/42432>.
  31. Yin, P., C. J. Burns, ..., B. A. Cornell. 2003. A tethered bilayer sensor containing alamethicin channels and its detection of amiloride based inhibitors. *Biosens. Bioelectron.* 18:389–397. [https://doi.org/10.1016/s0956-5663\(02\)00160-4](https://doi.org/10.1016/s0956-5663(02)00160-4).
  32. Matsuno, N., M. Murawsky, ..., J. Cuppoletti. 2004. Solid support membranes for ion channel arrays and sensors: application to rapid screening of pharmacological compounds. *Biochim. Biophys. Acta Biomembr.* 1665:184–190. <https://doi.org/10.1016/j.bbmem.2004.07.010>.
  33. Blake, S., T. Mayer, ..., J. Yang. 2006. Monitoring chemical reactions by using ion-channel-forming peptides. *ChemBioChem.* 7:433–435. <https://doi.org/10.1002/cbic.200500532>.
  34. Grieshaber, D., R. MacKenzie, ..., E. Reimhult. 2008. Electrochemical biosensors - sensor principles and architectures. *Sensors.* 8:1400–1458. <https://doi.org/10.3390/s8031400>.
  35. Cevc, G. 1990. Membrane electrostatics. *Biochim. Biophys. Acta.* 1031:311–382. [https://doi.org/10.1016/0304-4157\(90\)90015-5](https://doi.org/10.1016/0304-4157(90)90015-5).
  36. Clarke, R. J. 2001. The dipole potential of phospholipid membranes and methods for its detection. *Adv. Colloid Interface Sci.* 89-90:263–281. [https://doi.org/10.1016/s0001-8686\(00\)00061-0](https://doi.org/10.1016/s0001-8686(00)00061-0).
  37. Wang, L. 2012. Measurements and implications of the membrane dipole potential. *Annu. Rev. Biochem.* 81:615–635. <https://doi.org/10.1146/annurev-biochem-070110-123033>.
  38. Kintzer, A. F., E. M. Green, ..., R. M. Stroud. 2018. Structural basis for activation of voltage sensor domains in an ion channel TPC1. *Proc. Natl. Acad. Sci. U S A.* 115:E9095–E9104. <https://doi.org/10.1073/pnas.1805651115>.
  39. Groome, J. R., and L. Bayless-Edwards. 2020. Roles for countercharge in the voltage sensor domain of ion channels. *Front. Pharmacol.* 11. <https://doi.org/10.3389/fphar.2020.00160>.
  40. Richardson, B. D., K. Saha, ..., H. Khoshbouei. 2016. Membrane potential shapes regulation of dopamine transporter trafficking at the plasma membrane. *Nat. Commun.* 7:10423. <https://doi.org/10.1038/ncomms10423>.
  41. Zorova, L. D., V. A. Popkov, ..., D. B. Zorov. 2018. Mitochondrial membrane potential. *Anal. Biochem.* 552:50–59. <https://doi.org/10.1016/j.ab.2017.07.009>.
  42. Murata, Y., H. Iwasaki, ..., Y. Okamura. 2005. Phosphoinositide phosphatase activity coupled to an intrinsic voltage sensor. *Nature.* 435:1239–1243. <https://doi.org/10.1038/nature03650>.
  43. Kim, B. L., N. P. Schafer, and P. G. Wolynes. 2014. Predictive energy landscapes for folding  $\alpha$ -helical transmembrane proteins. *Proc. Natl. Acad. Sci. U S A.* 111:11031–11036. <https://doi.org/10.1073/pnas.1410529111>.
  44. Zhang, X. C., and H. Li. 2019. Interplay between the electrostatic membrane potential and conformational changes in membrane proteins. *Protein Sci.* 28:502–512. <https://doi.org/10.1002/pro.3563>.
  45. Copeland, B. R., R. Landick, ..., D. L. Oxender. 1984. Role of membrane potential in protein folding and domain formation during secretion in *Escherichia coli*. *J. Cell. Biochem.* 24:345–356. <https://doi.org/10.1002/jcb.240240405>.
  46. Sato, T. K., S. Kawano, and T. Endo. 2019. Role of the membrane potential in mitochondrial protein unfolding and import. *Sci. Rep.* 9:7637. <https://doi.org/10.1038/s41598-019-44152-z>.
  47. Wang, S., J. Zhang, ..., M. E. Orazem. 2021. Electrochemical impedance spectroscopy. *Nat. Rev. Methods Primers.* 1:41. <https://doi.org/10.1038/s43586-021-00039-w>.
  48. Karedla, N., A. M. Chizhik, ..., J. Enderlein. 2018. Three-dimensional single-molecule localization with nanometer accuracy using Metal-Induced Energy Transfer (MIET) imaging. *J. Chem. Phys.* 148:204201. <https://doi.org/10.1063/1.5027074>.
  49. Gregor, I., A. Chizhik, ..., J. Enderlein. 2019. Metal-induced energy transfer. *Nanophotonics.* 8:1689–1699. <https://doi.org/10.1515/nanoph-2019-0201>.
  50. Nečas, D., and P. Klapeček. 2012. Gwyddion: an open-source software for SPM data analysis. *Cen. Eur. J. Phys.* 10:181–188.
  51. Leventis, P. A., and S. Grinstein. 2010. The distribution and function of phosphatidylserine in cellular membranes. *Annu. Rev. Biophys.* 39:407–427. <https://doi.org/10.1146/annurev.biophys.093008.131234>.
  52. Santra, K., J. Zhan, ..., J. W. Petrich. 2016. What is the best method to fit time-resolved data? A comparison of the residual minimization and the maximum likelihood techniques as applied to experimental time-correlated, single-photon counting data. *J. Phys. Chem. B.* 120:2484–2490. <https://doi.org/10.1021/acs.jpcc.6b00154>.
  53. Dymond, A. M. 1976. Characteristics of the metal-tissue interface of stimulation electrodes. *IEEE Trans. Biomed. Eng.* 23:274–280. <https://doi.org/10.1109/tbme.1976.324585>.
  54. Enderlein, J. 2000. A theoretical investigation of single-molecule fluorescence detection on thin metallic layers. *Biophys. J.* 78:2151–2158. [https://doi.org/10.1016/s0006-3495\(00\)76761-0](https://doi.org/10.1016/s0006-3495(00)76761-0).
  55. Aygun, G., and R. Turan. 2008. Electrical and dielectric properties of tantalum oxide films grown by Nd:YAG laser assisted oxidation. *Thin Solid Films.* 517:994–999. <https://doi.org/10.1016/j.tsf.2008.07.039>.
  56. Leng, Y. X., J. Chen, ..., N. Huang. 2006. The biocompatibility of the tantalum and tantalum oxide films synthesized by pulse metal vacuum arc source deposition. *Nucl. Instrum. Methods Phys. Res. B.* 242:30–32. <https://doi.org/10.1016/j.nimb.2005.08.002>.
  57. Tero, R. 2012. Substrate effects on the formation process, structure and physicochemical properties of supported lipid bilayers. *Materials.* 5:2658–2680. <https://doi.org/10.3390/ma5122658>.
  58. Seu, K. J., A. P. Pandey, ..., J. S. Hovis. 2007. Effect of surface treatment on diffusion and domain formation in supported lipid bilayers. *Biophys. J.* 92:2445–2450. <https://doi.org/10.1529/biophysj.106.099721>.
  59. Khademi, M., and D. P. J. Barz. 2020. Structure of the electrical double layer revisited: electrode capacitance in aqueous solutions. *Langmuir.* 36:4250–4260. <https://doi.org/10.1021/acs.langmuir.0c00024>.
  60. Montal, M., and P. Mueller. 1972. formation of bimolecular membranes from lipid monolayers and a study of their electrical properties.

- Proc. Natl. Acad. Sci. U S A.* 69:3561–3566. <https://doi.org/10.1073/pnas.69.12.3561>.
61. Valincius, G., T. Meškauskas, and F. Ivanauskas. 2012. Electrochemical impedance spectroscopy of tethered bilayer membranes. *Langmuir*. 28:977–990. <https://doi.org/10.1021/la204054g>.
  62. Simeonova, M., and J. Gimsa. 2006. The influence of the molecular structure of lipid membranes on the electric field distribution and energy absorption. *Bioelectromagnetics*. 27:652–666. <https://doi.org/10.1002/bem.20259>.
  63. Merla, C., A. Denzi, ..., M. Liberti. 2012. Novel passive element circuits for microdosimetry of nanosecond pulsed electric fields. *IEEE Trans. Biomed. Eng.* 59:2302–2311. <https://doi.org/10.1109/tbme.2012.2203133>.
  64. Poltorak, L., M. L. Verheijden, ..., E. J. Sudhölter. 2018. Lipid bilayers cushioned with polyelectrolyte-based films on doped silicon surfaces. *Biochim. Biophys. Acta Biomembr.* 1860:2669–2680. <https://doi.org/10.1016/j.bbamem.2018.09.018>.
  65. Chang, W. K., W. C. Wimley, ..., M. Merzlyakov. 2008. Characterization of antimicrobial peptide activity by electrochemical impedance spectroscopy. *Biochim. Biophys. Acta Biomembr.* 1778:2430–2436. <https://doi.org/10.1016/j.bbamem.2008.06.016>.
  66. Krishna, G., J. Schulte, ..., P. D. Osman. 2003. Tethered bilayer membranes containing ionic reservoirs: selectivity and conductance. *Langmuir*. 19:2294–2305. <https://doi.org/10.1021/la026238d>.
  67. Gomez, E. W., N. G. Clack, ..., J. T. Groves. 2009. Like-charge interactions between colloidal particles are asymmetric with respect to sign. *Soft Matter*. 5:1931. <https://doi.org/10.1039/b821510c>.
  68. McLaughlin, S. 1989. The electrostatic properties of membranes. *Annu. Rev. Biophys. Biophys. Chem.* 18:113–136. <https://doi.org/10.1146/annurev.bb.18.060189.000553>.
  69. Gross, E., R. S. Bedlack, and L. M. Loew. 1994. Dual-wavelength ratiometric fluorescence measurement of the membrane dipole potential. *Biophys. J.* 67:208–216. [https://doi.org/10.1016/s0006-3495\(94\)80471-0](https://doi.org/10.1016/s0006-3495(94)80471-0).
  70. Chachaj-Brekiesz, A., J. Kobierski, ..., P. Dynarowicz-Latka. 2021. Electrical properties of membrane phospholipids in Langmuir monolayers. *Membranes*. 11:53. <https://doi.org/10.3390/membranes11010053>.
  71. Klausen, L. H., T. Fuhs, and M. Dong. 2016. Mapping surface charge density of lipid bilayers by quantitative surface conductivity microscopy. *Nat. Commun.* 7:12447. <https://doi.org/10.1038/ncomms12447>.
  72. Ochmann, S. E., T. Schröder, ..., P. Tinnefeld. 2022. Quantitative single-molecule measurements of membrane charges with DNA origami sensors. *Anal. Chem.* 94:2633–2640. <https://doi.org/10.1021/acs.analchem.1c05092>.
  73. Salzberg, B. M., H. V. Davila, and L. B. Cohen. 1973. Optical recording of impulses in individual neurones of an invertebrate central nervous system. *Nature*. 246:508–509. <https://doi.org/10.1038/246508a0>.
  74. Montana, V., D. L. Farkas, and L. M. Loew. 1989. Dual-wavelength ratiometric fluorescence measurements of membrane potential. *Biochemistry*. 28:4536–4539. <https://doi.org/10.1021/bi00437a003>.
  75. M. Canepari and D. Zecevic, eds 2011. *Membrane Potential Imaging in the Nervous System*. Springer-Verlag.
  76. Miller, E. W. 2016. Small molecule fluorescent voltage indicators for studying membrane potential. *Curr. Opin. Chem. Biol.* 33:74–80. <https://doi.org/10.1016/j.cbpa.2016.06.003>.
  77. Miller, E. W., J. Y. Lin, ..., R. Y. Tsien. 2012. Optically monitoring voltage in neurons by photo-induced electron transfer through molecular wires. *Proc. Natl. Acad. Sci. U S A.* 109:2114–2119. <https://doi.org/10.1073/pnas.1120694109>.
  78. Lazzari-Dean, J. R., A. M. Gest, and E. W. Miller. 2019. Optical estimation of absolute membrane potential using fluorescence lifetime imaging. *eLife*. 8:e44522. <https://doi.org/10.7554/elife.44522>.
  79. Woodford, C. R., E. P. Frady, ..., R. Y. Tsien. 2015. Improved PeT molecules for optically sensing voltage in neurons. *J. Am. Chem. Soc.* 137:1817–1824. <https://doi.org/10.1021/ja510602z>.
  80. Raguse, B., V. Braach-Maksyvytis, ..., L. Wiczorek. 1998. Tethered lipid bilayer membranes: formation and ionic reservoir characterization. *Langmuir*. 14:648–659. <https://doi.org/10.1021/la9711239>.
  81. Enderlein, J. 1999. Single-molecule fluorescence near a metal layer. *Chem. Phys.* 247:1–9. [https://doi.org/10.1016/s0301-0104\(99\)00097-x](https://doi.org/10.1016/s0301-0104(99)00097-x).
  82. Berndt, M., M. Lorenz, ..., S. Diez. 2010. Axial nanometer distances measured by fluorescence lifetime imaging microscopy. *Nano Lett.* 10:1497–1500. <https://doi.org/10.1021/nl100593x>.
  83. Chizhik, A. I., A. M. Chizhik, ..., J. Enderlein. 2011. Probing the radiative transition of single molecules with a tunable microresonator. *Nano Lett.* 11:1700–1703. <https://doi.org/10.1021/nl200215v>.
  84. Kulkarni, R. U., H. Yin, ..., E. W. Müller. 2017. A rationally designed, general strategy for membrane orientation of photoinduced electron transfer-based voltage-sensitive dyes. *ACS Chem. Biol.* 12:407–413. <https://doi.org/10.1021/acscchembio.6b00981>.
  85. Ghosh, A., A. Sharma, ..., J. Enderlein. 2019. Graphene-based metal-induced energy transfer for sub-nanometre optical localization. *Nat. Photonics*. 13:860–865. <https://doi.org/10.1038/s41566-019-0510-7>.
  86. Li, L.-S. 2007. Fluorescence probes for membrane potentials based on mesoscopic electron transfer. *Nano Lett.* 7:2981–2986. <https://doi.org/10.1021/nl071163p>.
  87. Ha, T., T. Enderle, ..., S. Weiss. 1996. Probing the interaction between two single molecules: fluorescence resonance energy transfer between a single donor and a single acceptor. *Proc. Natl. Acad. Sci. U S A.* 93:6264–6268. <https://doi.org/10.1073/pnas.93.13.6264>.
  88. Loura, L. M. S., and M. Prieto. 2011. FRET in membrane biophysics: an overview. *Front. Physiol.* 2:82. <https://doi.org/10.3389/fphys.2011.00082>.
  89. Lerner, E., T. Cordes, ..., S. Weiss. 2018. Toward dynamic structural biology: two decades of single-molecule Förster resonance energy transfer. *Science*. 359:eaan1133. <https://doi.org/10.1126/science.aan1133>.
  90. Mazal, H., and G. Haran. 2019. Single-molecule FRET methods to study the dynamics of proteins at work. *Curr. Opin. Biomed. Eng.* 12:8–17. <https://doi.org/10.1016/j.cobme.2019.08.007>.
  91. Bartels, K., T. Lasitzka-Male, ..., C. Löw. 2021. Single-molecule FRET of membrane transport proteins. *ChemBioChem*. 22:2657–2671. <https://doi.org/10.1002/cbic.202100106>.
  92. Füllbrunn, N., Z. Li, ..., C. You. 2021. Nanoscopic anatomy of dynamic multi-protein complexes at membranes resolved by graphene-induced energy transfer. *eLife*. 10:e62501. <https://doi.org/10.7554/elife.62501>.
  93. Zanut, A., A. Fiorani, ..., G. Valenti. 2019. Electrochemiluminescence as emerging microscopy techniques. *Anal. Bioanal. Chem.* 411:4375–4382. <https://doi.org/10.1007/s00216-019-01761-x>.
  94. Dong, J., Y. Lu, ..., J. Feng. 2021. Direct imaging of single-molecule electrochemical reactions in solution. *Nature*. 596:244–249. <https://doi.org/10.1038/s41586-021-03715-9>.
  95. Namink, K., X. Meng, ..., S. Faez. 2020. Electric-double-layer-modulation microscopy. *Phys. Rev. Appl.* 13:044065. <https://doi.org/10.1103/physrevapplied.13.044065>.
  96. Saqib, M., Y. Fan, ..., B. Zhang. 2021. Optical imaging of nanoscale electrochemical interfaces in energy applications. *Nano Energy*. 90:106539. <https://doi.org/10.1016/j.nanoen.2021.106539>.
  97. Murphy, B. D., and A. A. J. Torriero. 2018. Critical overview of the use of tethered bilayer lipid membranes with electrochemical techniques. *Med. Anal. Chem. Int. J.* 2. <https://doi.org/10.23880/macij-16000110>.
  98. Picas, L., P.-E. Milhiet, and J. Hernández-Borrell. 2012. Atomic force microscopy: a versatile tool to probe the physical and chemical properties of supported membranes at the nanoscale. *Chem. Phys. Lipids*. 165:845–860. <https://doi.org/10.1016/j.chemphyslip.2012.10.005>.

99. Naumowicz, M., and Z. A. Figaszewski. 2005. Impedance analysis of lipid domains in phosphatidylcholine bilayer membranes containing ergosterol. *Biophys. J.* 89:3174–3182. <https://doi.org/10.1529/biophysj.105.063446>.
100. Svetlova, A., J. Ellieroth, ..., A. Offenhäusser. 2019. Composite lipid bilayers from cell membrane extracts and artificial mixes as a cell culture platform. *Langmuir*. 35:8076–8084. <https://doi.org/10.1021/acs.langmuir.9b00763>.
101. Flynn, K. R., A. Sutti, ..., A. A. Torriero. 2018. Critical effects of polar fluorescent probes on the interaction of DHA with POPC supported lipid bilayers. *Biochim. Biophys. Acta Biomembr.* 1860:1135–1142. <https://doi.org/10.1016/j.bbamem.2018.01.013>.
102. Alghalayini, A., A. Garcia, ..., C. Cranfield. 2019. The use of tethered bilayer lipid membranes to identify the mechanisms of antimicrobial peptide interactions with lipid bilayers. *Antibiotics*. 8:12. <https://doi.org/10.3390/antibiotics8010012>.
103. Andersson, J., I. Köper, and W. Knoll. 2018. Tethered membrane architectures—design and applications. *Front. Mater.* 5. <https://doi.org/10.3389/fmats.2018.00055>.
104. Andersson, J., and I. Köper. 2016. Tethered and polymer supported bilayer lipid membranes: structure and function. *Membranes*. 6:30. <https://doi.org/10.3390/membranes6020030>.
105. Cranfield, C. G., B. Cornell, ..., B. Martinac. 2014. Transient potential gradients and impedance measures of tethered bilayer lipid membranes: pore-forming peptide insertion and the effect of electroporation. *Biophys. J.* 106:182–189. <https://doi.org/10.1016/j.bpj.2013.11.1121>.
106. Valincius, G., and M. Mickevicius. 2015. Chapter two - tethered phospholipid bilayer membranes: an interpretation of the electrochemical impedance response. *In Advances in Planar Lipid Bilayers and Liposomes*. A. Igljić, C. V. Kulkarni, and M. Rappolt, eds. Academic Press, pp. 27–61.
107. Lin, J., J. Szymanski, ..., K. Hristova. 2010. Electrically addressable, biologically relevant surface-supported bilayers. *Langmuir*. 26:12054–12059. <https://doi.org/10.1021/la101084b>.